


Nonadiabatic storage of short light pulses in an atom-cavity system

Tobias Macha ^{*}, Eduardo Uruñuela, Wolfgang Alt, Maximilian Ammenwerth, Deepak Pandey, Hannes Pfeifer, and Dieter Meschede

Institut für Angewandte Physik, Universität Bonn, Wegelerstraße 8, 53115 Bonn, Germany



(Received 8 April 2019; revised manuscript received 6 April 2020; accepted 6 April 2020; published 4 May 2020)

We demonstrate the storage of 5-ns light pulses in a single rubidium atom coupled to a fiber-based optical resonator. Our storage protocol addresses a regime beyond the conventional adiabatic limit and approaches the theoretical bandwidth limit. We extract the optimal control laser pulse properties from a numerical simulation of our system and measure storage efficiencies of $(8.1 \pm 1.1)\%$, in close agreement with the maximum expected efficiency. Such well-controlled and high-bandwidth atom-photon interfaces are key components for future hybrid quantum networks.

DOI: [10.1103/PhysRevA.101.053406](https://doi.org/10.1103/PhysRevA.101.053406)

I. INTRODUCTION

Quantum networks are the basis for distributed quantum information processing [1–3] and long-distance quantum communication [4,5]. In quantum networks [6], distant nodes are connected via quantum channels, e.g., optical fibers guiding single photons as flying qubits [7]. The nodes for processing and storage of quantum information require long coherence times and the ability to efficiently convert flying to stationary qubits and vice versa. Single atoms in optical cavities have shown to fulfill these criteria [8,9], but so far only in the adiabatic regime of atom-cavity dynamics when interacting with photon pulses of length $T \gg \kappa/g^2$, where κ is the cavity bandwidth and g is the atom-cavity coupling strength. Both working in this regime and the choice of cavity parameters have limited previous experiments to pulses much longer than the atomic excited-state lifetime τ_e and the cavity field decay time [9,10]. However, high-bandwidth quantum communication will use short pulses, such as the polarization-entangled photons emitted by quantum dots [11] or spontaneous parametric down-conversion sources [12].

In our approach, we use a high-bandwidth, microscopic fiber Fabry-Pérot cavity (FFPC) [13], strongly coupled to a single atom, to store a weak coherent pulse in the nonadiabatic regime near $T \sim \kappa/g^2$ [14]. This way, pulses with $T \ll \tau_e$ are stored, which is not possible in free space [15,16]. The cavity is thus used as a bandwidth converter, matching the narrow atomic transition to a spectrally broad pulse near the cavity-bandwidth limit $T^{-1} \sim \kappa$. The pulse is mapped into the atomic ground states with the help of a control laser in Raman configuration. In order to execute the storage process efficiently, the exact control pulse properties, such as the temporal profile, have to be found and matched to the input pulse. Prominent theoretical work [14,17,18] has been mostly concerned with realizing an adiabatic state transfer during the storage process and hence is not applicable in our case. Instead, we determine an optimum pulse sequence in the

nonadiabatic storage regime by numerical simulations based on the full quantum-mechanical Lindblad master equation describing our system. As a result, we reach an excellent agreement between expected and measured storage efficiencies.

II. EXPERIMENTAL SETUP

Our photon memory consists of a single ^{87}Rb atom trapped at the center of a single-sided, high-bandwidth FFPC [19]. One of the fiber mirrors presents a higher transmission (HT), ensuring a highly directional input-output channel [20]. As depicted in Fig. 1(a), the cavity is placed at the focus of four in-vacuum, aspheric lenses (NA = 0.5), which lead to a high beam-pointing stability [21]. The lenses strongly focus two pairs of counterpropagating, red-detuned dipole trap beams at 860 nm which create a two-dimensional optical lattice in the xy plane, see Fig. 1(b). One of the lattices acts as a conveyor belt [22] to transport atoms from a magneto-optical trap (MOT) into the cavity. Confinement in the z direction is provided by the intracavity, blue-detuned lock laser field at 770 nm, which is additionally used for stabilizing the resonator length and for carrier-free Raman cooling in three dimensions [23,24]. As a result, the atom is located with subwavelength precision at an antinode of the cavity mode driven by the input pulse. In particular, the mode is resonant to the Stark-shifted $|F = 2, m_F = -2\rangle \rightarrow |F' = 2, m_F = -1\rangle$ hyperfine transition of rubidium at 780 nm. The quantization axis is aligned with the cavity axis by applying a magnetic guiding field of ~ 1.8 G.

In each experimental cycle, the memory is initialized by cooling and preparing the atom in the state $|F = 2, m_F = -2\rangle$ by optical pumping with an efficiency exceeding 95%. As a first step of the storage protocol, we send a triggered, coherent input pulse with a mean photon number n and a duration of 5 ns (FWHM). It has a time-symmetric, sine-squared shaped probability amplitude $|\phi_{\text{in}}(t)|$ of the electric field [6]. When it enters the FFPC through the HT mirror, a classical control laser pulse in two-photon resonance is simultaneously applied from the side along the x axis [Fig. 1(b)]. This results in

^{*}macha@iap.uni-bonn.de

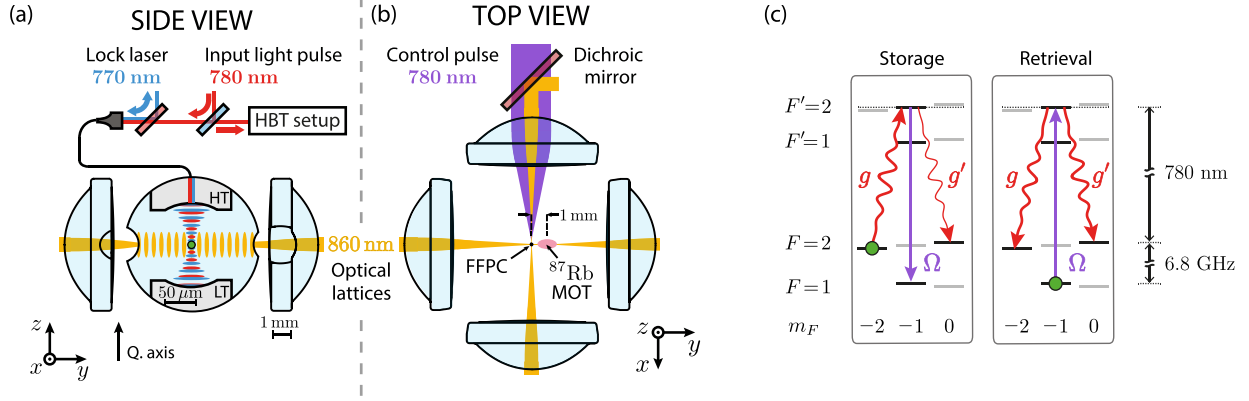


FIG. 1. Schematic side (a) and top (b) views of the experimental setup illustrate the optical lattices trapping a single rubidium (^{87}Rb) atom at the center of a microscopic fiber Fabry-Pérot cavity (FFPC). The high-transmission (HT) mirror of the cavity is the access port for a coherent input light pulse, which is stored in the atomic memory via a control pulse entering from the side. Retrieved single photons are guided to a Hanbury Brown-Twiss (HBT) setup for detection. (c) Photon storage for a cavity with two degenerate polarization modes. The first mode couples the initial state $|F, m_F\rangle = |2, -2\rangle$ to the excited state $|2', -1\rangle$ with a rate g and either results in coherent transfer to $|1, -1\rangle$ by the interaction with the control laser (Rabi frequency Ω) or in coherent leakage to $|2, 0\rangle$ via a second cavity mode with rate g' . The efficiency of an adiabatic retrieval process is not affected, as the photon detection is polarization insensitive.

transferring the atom dominantly to the state $|F = 1, m_F = -1\rangle$, see Fig. 1(c). After a storage time of $1 \mu\text{s}$, the photon is read out with an adiabatic control pulse to ensure maximum population transfer [25–27]. The cycle of state initialization, photon storage, and retrieval is repeated with the same atom up to 1500 times for ~ 2 s, limited by the efficiency of the currently employed cooling mechanism.

III. RESULTS

To find the optimum storage-assisting control laser pulse with time-dependent Rabi frequency $\Omega(t)$, we simulate the system based on a Lindblad master equation. The underlying Hamiltonian consists of the Jaynes-Cummings Hamiltonian [28] and an additional driving term

$$\hat{H}_d(t) = i\hbar \frac{\Omega(t)}{2} (\hat{\sigma}^\dagger - \hat{\sigma}) + \hbar \sqrt{2\kappa_{\text{HT}}} \cdot \sqrt{n} \cdot \phi_{\text{in}}(t) (\hat{a}^\dagger + \hat{a}),$$

where $\hat{\sigma}^\dagger, \hat{\sigma}$ are the flip operators of the atomic states that are coupled via $\Omega(t)$, while $\hat{a}^\dagger(\hat{a})$ is the creation (annihilation) operator of the driven cavity mode. The total cavity damping $\kappa = \kappa_{\text{HT}} + \kappa_{\text{loss}}$ is the sum of the pure transmission rate κ_{HT} at which a coherent field $[\phi_{\text{in}}(t)]$ impinging on the HT mirror interacts with the open system, and the undesired losses κ_{loss} , e.g., due to absorption and scattering on the mirrors (for more details see Appendix).

Our cavity supports two degenerate polarization modes (σ^\pm), which couple two Zeeman states in the same hyperfine manifold $F = 2$ via the excited state $|2', -1\rangle$ [Fig. 1(c)]. With the π -polarized control laser coupling the excited state to the $F = 1$ manifold, our choice of the initial Zeeman state leads to coherent dynamics in a tripod configuration [29]. Additionally, the probability to off-resonantly excite the state $|1', -1\rangle$ has to be considered. We take all of these effects into account in our model by including two polarization cavity modes with effective atom-cavity coupling strengths g, g' and a total of five atomic states (for a detailed discussion see Appendix).

The main effect of the ideally absent atom-cavity coupling g' is a coherent population leakage during a storage attempt. The photon storage efficiency η_{storage} , which is the transfer efficiency η_{transfer} from the initial to the target state normalized by the mean input photon number ($\eta_{\text{storage}} = \eta_{\text{transfer}}/n$), is thus decreased compared to a standard Λ configuration [14].

In general, the storage efficiency depends crucially on the properties of the control pulse, namely, the temporal shape, the pulse amplitude, the detuning from the atomic transition, and the delay with respect to the input pulse. However, in a nonadiabatic regime we find that its exact temporal shape plays a minor role. A simple compression of the temporal length of the pulse shape for the adiabatic protocol [18] is equally effective as a numerically optimized pulse shape for our short input pulse [30]. In case of zero single-photon detuning of the input pulse with respect to the atomic excited state, our simulation predicts the highest storage efficiency for a vanishing two-photon detuning of the Raman transition, as also predicted by [14]. The remaining pulse parameters for optimal storage are the peak Rabi frequency of the control laser and its delay τ_Ω with respect to the input light pulse.

Besides the pulse parameters, knowledge about the system parameters $g, g', \kappa_{\text{HT}}, \kappa_{\text{loss}}, \gamma$ is important for the storage process. κ_{HT} is known from the mirror characterization in [20], and $\kappa_{\text{loss}} = \kappa - \kappa_{\text{HT}}$ is obtained after measuring κ by probing the frequency-dependent cavity reflection. For determining g, g' , we take a measurement during which we store an input pulse with on average $n = 2.1$ photons and reconstruct the retrieved pulse after the memory readout, as shown in Fig. 2. A simulation-based fit of the resulting shape with g, g' as free parameters completes our set of system parameters: $(g, g', \kappa_{\text{HT}}, \kappa_{\text{loss}}, \gamma) = 2\pi \times (29, 35, 16, 25, 3)$ MHz.

Two additional measurements determine the coherent storage fraction. The first one omits the control pulse during the storage process and thus indicates the incoherent state transfer due to optical pumping by the input pulse. The second measurement uses neither control nor input pulse, which

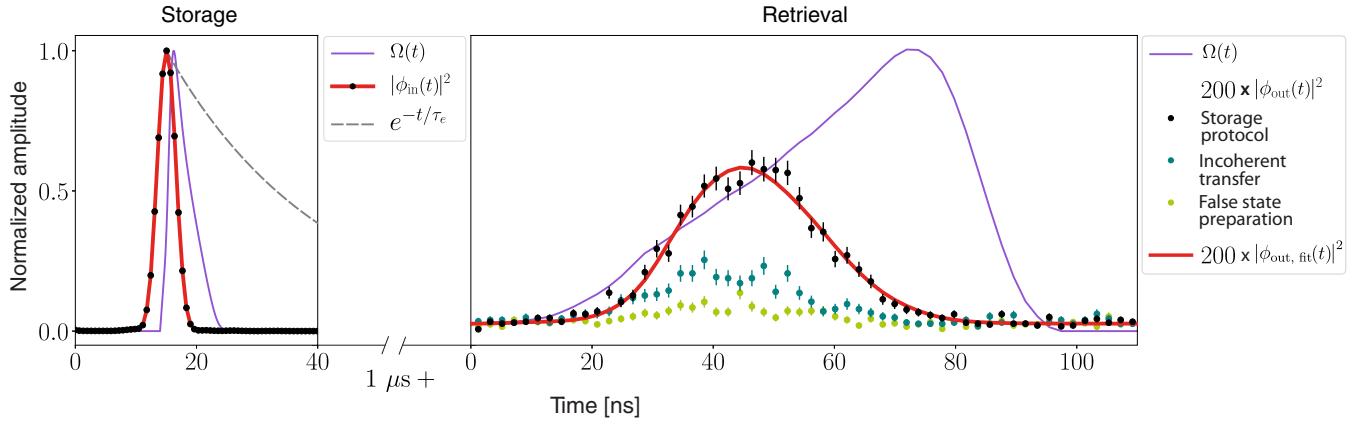


FIG. 2. On the left: The time-symmetric, sine-squared shaped input pulse with intensity probability amplitude $|\phi_{\text{in}}(t)|^2$ sent to the HT mirror has a FWHM duration of 5 ns (black points connected by red, solid line). For comparison, the atomic excited state decays with a time constant of $\tau_e = 26$ ns is shown (gray, dashed line). The Raman control pulse with Rabi frequency $\Omega(t)$ (purple, solid line) is applied with a delay of 4 ns with respect to the input pulse, in contrast to adiabatic storage protocols (see main text). All pulse amplitudes are normalized to 1. On the right: After a storage time of $1 \mu\text{s}$, a control pulse (purple, solid line) adiabatically generates a photon $|\phi_{\text{out}}(t)|^2$ after the full storage protocol (black dots). By taking into account the incoherently transferred population in the absence of a control pulse (dark green dots) and the counts due to false initial state preparation (bright green dots), we infer a coherent storage component of $(79 \pm 3)\%$. The data-point values have been scaled by a factor of 200, while the Raman pulse is still normalized to 1. From a simulation-based fit $|\phi_{\text{out, fit}}(t)|^2$ (red, solid line) we extract the atom-cavity coupling strengths $(g, g') = 2\pi \times (29, 35)$ MHz.

indicates false state preparation. From the ratio of the integrated detection counts in Fig. 2, we obtain a coherent storage component of $(79 \pm 3)\%$ (for the special case of $n = 2.1$). In a Hanbury Brown–Twiss experiment we verify the single-photon character of the retrieved pulses by calculating the correlation function $g_c^{(2)}(0) = (12.2 \pm 6.5)\%$ from the time trace of detected photons, see Fig. 3. The value is consistent with the amount of background light and detector dark counts (see Appendix).

In a next step, the previously obtained system parameters are used to simulate the storage process in order to map out the full parameter space for the optimization of the storage efficiency η_{storage} . In Fig. 4(a), η_{storage} is displayed as a function of the peak Rabi frequency of the control laser and its delay τ_Ω , and in Fig. 4(b), the transfer efficiency η_{transfer} as a function of the peak Rabi frequency and mean photon number per input pulse is shown. The latter is of interest for cross-checking the

photon number calibration, which is required to determine the storage efficiency rather than the transfer efficiency.

The simulation results show efficiency revivals towards higher Rabi frequencies, which give insight into the underlying storage process. The revivals are a consequence of the excited state being significantly populated before it is mapped by the control laser to the target ground state in a coherent π -pulse interaction [14]. In contrast, a classic stimulated Raman adiabatic passage (STIRAP) protocol [31] does not show revivals. It relies on the adiabatic transfer between the ground states, which is no longer the most efficient storage method in the presented experiment.

We confirm the simulated behavior by measuring four independent parameter scans, which are fitted to the experimentally accessible regions of the two simulated maps. To obtain the storage and transfer efficiencies from the measurement, the photon detection probabilities per storage attempt are corrected for the imperfect state preparation, the read-out efficiency of $(80 \pm 5)\%$, the escape efficiency $\kappa_{\text{HT}}/\kappa = (39 \pm 1)\%$, the transmission in the optical path, the detection efficiencies of $(17 \pm 2)\%$, and the spatial mode matching between fiber-guided and cavity mode of $(60 \pm 2)\%$ [20]. For an input pulse with $n = 1$ [see Fig. 4(a)] we observe a maximum while scanning the control laser peak Rabi frequency, from which we deduce the storage efficiency of $\eta_{\text{storage}} = (8.1 \pm 1.1)\%$, which is close to the highest expected value of 9.0% for our tripod system with cavity losses. Taking the aforementioned efficiencies into account, the end-to-end efficiency of creating an outgoing single-photon Fock state per impinging coherent state is $(0.9 \pm 0.1)\%$. For larger mean photon numbers per pulse [see Fig. 4(b)], we observe the expected saturation of the transfer efficiency, which is limited by the undesired transfer to $|2, 0\rangle$ (see also Appendix). However, for higher peak Rabi frequencies the measured data deviates from the simulation [Fig. 4(b)]. We attribute

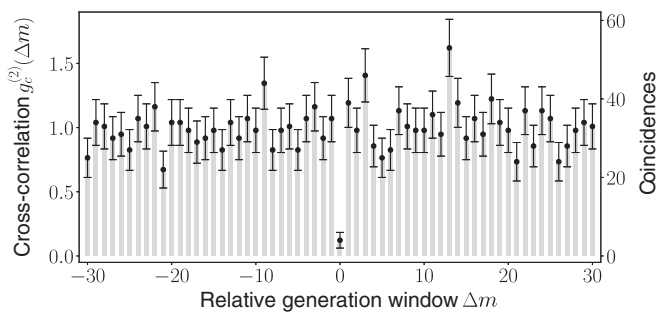


FIG. 3. We verify the single-photon character of the cavity emission by calculating the cross correlation $g_c^{(2)}$ of photons detected by the HBT setup, which is depicted in Fig. 1(a). We observe a minimum of $g_c^{(2)}(0) = (12.2 \pm 6.5)\%$, which is intrinsically limited to $g_{\text{c,bg}}^{(2)}(0) \approx (13.6 \pm 0.1)\%$ by detector dark- and background counts (see Appendix).

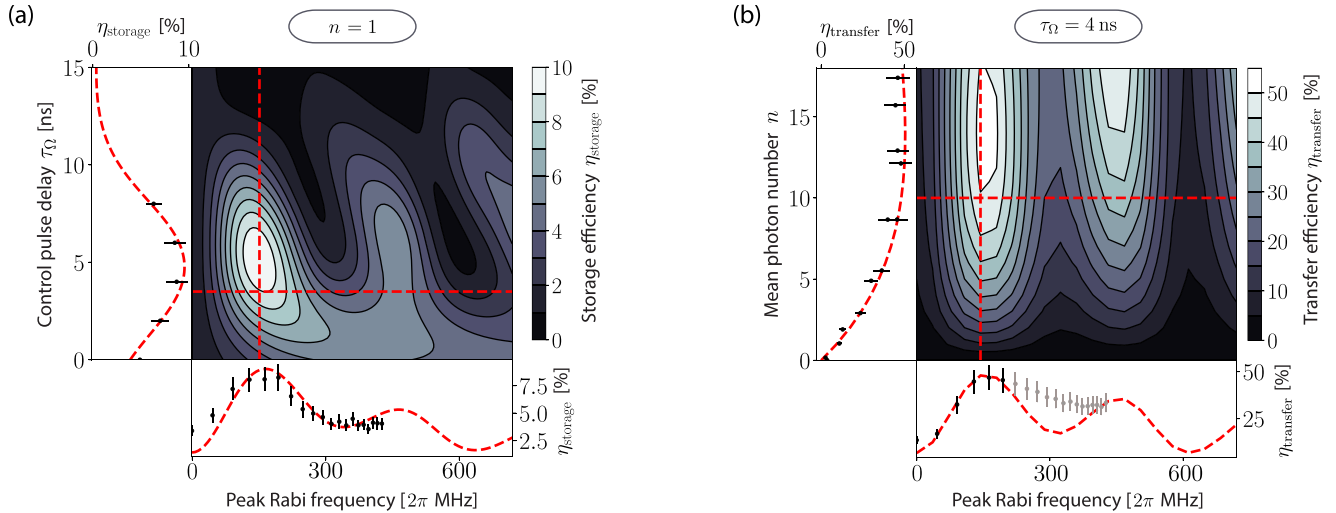


FIG. 4. Simulated efficiency maps and experimental pulse parameter scans. (a) For an input pulse containing a mean photon number of $n = 1$, the storage efficiency η_{storage} as a function of both control pulse peak Rabi frequency and control pulse delay τ_{Ω} is simulated. The nonadiabatic storage process reveals a significant atomic excited-state population, which is then mapped by the control laser to the target ground state in a coherent π -pulse process. Thus, for higher peak Rabi frequencies efficiency revivals are observed. (b) For a fixed control pulse delay of 4 ns, the transfer efficiency η_{transfer} is simulated as a function of both control pulse peak Rabi frequency and mean photon number per input pulse n . The measured transfer and storage efficiencies for four independent, experimental parameter scans (black points) are fitted to the simulation of our system (red, dashed lines). This allows us to extract the storage efficiency $\eta_{\text{storage}} = (8.2 \pm 0.6)\%$ for a coherent input pulse with a mean photon number of $n = 1$. The error bars combine both statistical and systematic uncertainties. Data points in gray are not considered by the fit (see main text).

this behavior to variations in both the atom-cavity coupling strength and the AC Stark shift, which originate from different atom positions within the cavity mode and dipole traps. As a result, the optimum (two-photon) Rabi frequency is met at higher peak Rabi frequencies than expected, leading to the observed higher efficiencies.

With technical improvements such as the realization of a three-level (Λ) configuration, the efficiency can already be improved by a factor of about 2. Assuming negligible undesired cavity losses, storage efficiencies exceeding 40% should be feasible with a single atom. The overall memory efficiency can be increased by fiber cavities equipped with graded index (GRIN) lenses [32], which reduce the losses due to a cavity-fiber mode-mismatch.

IV. CONCLUSION

In conclusion, we have demonstrated the nonadiabatic storage of light pulses, which are, with 5 ns, much shorter than the atomic excited-state lifetime of $\tau_e = 26$ ns. By simulating the storage process in dependence of the control pulse parameters, we find the optimum control pulse for the highest possible photon storage efficiency and, unlike many similar experiments, observe a remarkable agreement with experimentally obtained values.

Our system is capable of interacting with very short light pulses in a highly directional manner, thereby demonstrating functionality for a high-bandwidth quantum network. Additionally, FFPCs offer an intrinsic fiber coupling that facilitates the implementation in cavity-based networks [33,34]. We would like to point out that the storage of short pulses has been realized in warm atomic vapors [35] or atom-loaded

hollow-core fibers [36] as well, but here both the storage time at the single-photon level and the applications of the system are limited. In contrast, (few-) atom-cavity systems offer longer storage times [8] and are more versatile, e.g., for the realization of two-atom quantum gates [37].

In the future, we will employ ensembles of atoms, which will enhance the light-matter interaction by collective effects [38], allowing for storage of even shorter pulses with even higher bandwidths. In this way, true single-photon Fock states as provided by the emission of a quantum dot [11] can efficiently interact with our atom-based system. Envisioning such a hybrid experiment [39], we have recently demonstrated that the emission frequency of quantum dots can be stabilized to atomic transitions [40].

ACKNOWLEDGMENTS

This work has been funded by the Deutsche Forschungsgemeinschaft (DFG, German Research Foundation) through Project No. 277625399-TRR 185 and the Bundesministerium für Bildung und Forschung (BMBF) project Q.Link.X. We thank J. Gallego and E. Keiler for discussions and technical support in the early stage of the presented experiment.

APPENDIX A: EXPERIMENTAL METHODS

1. Tripod configuration

Here, we briefly explain the choice of the tripod configuration [29]. In our experiment, a few tens of neutral ^{87}Rb atoms are trapped from the background gas (10^{-10} mbar) and cooled in a magneto-optical trap which is located 1 mm away from the cavity center. An optical lattice acting as a conveyor

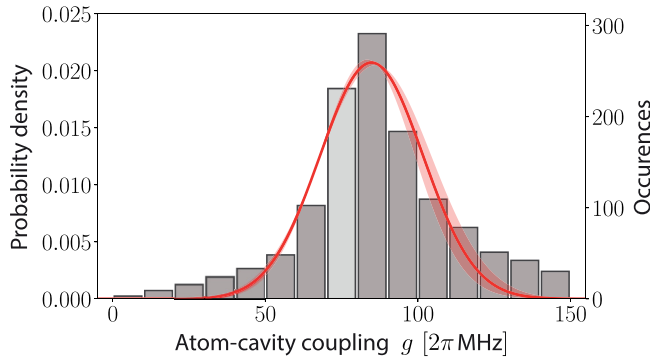


FIG. 5. The vacuum-Rabi splitting is measured to determine the individual atom-coupling strength g for each sequence repetition. The distribution of values is shown with a Gaussian fit and 1σ confidence intervals. Each value still has to be scaled by $\sqrt{1/6}$ to obtain the coupling strength on the $|2, -2\rangle \rightarrow |2', -1\rangle$ transition. As discussed in Appendix A, a specified range of coupling strengths (highlighted area) is used for postselection in Fig. 3 and for an accurate implementation of g in our simulations.

belt is used to transport them into the cavity region. Here, the presence of an atom is detected by its interaction with a near-resonant probe field at 780 nm, which is injected into the cavity via the HT mirror. This σ^- -polarized field drives the cycling transition $|F = 2, m_F = -2\rangle \rightarrow |F' = 3, m_F = -3\rangle$, which allows for a clean, nondestructive hyperfine state detection [41]. In the presence of a continuous repumper, which prepares the atom in its $F = 2$ ground-state manifold, the atomic presence is detected by an increase of the reflected probe light and the transport is stopped. At the same time, the probe and repumper also prepare the atom in $|F = 2, m_F = -2\rangle$, the chosen initial state for the storage protocol.

However, mapping the population between the two ground states via a Raman process [Fig. 1(c)] has to involve the excited state $F' = 2$ or $F' = 1$, so as a next step, we change the cavity length such that its resonance frequency is shifted by 267 MHz. Then the cavity mode is resonant with the $|F = 2, m_F = -2\rangle \rightarrow |F' = 2, m_F = -1\rangle$ transition, which is driven by the weak coherent light pulse. In the shifting process, we also measure the vacuum-Rabi splitting [42], from which we infer the atom-cavity coupling strength for each individual atom, see Fig. 5.

To make use of these well-established techniques for our experiment [19], the tripod configuration emerged as a first choice for the demonstration of short-light-pulse storage. However, for quantum memory applications it is not ideal. Our experiment therefore is a proof of principle for high-bandwidth applications and a milestone in the agreement between expected and measured efficiencies.

Besides that, the tripod configuration also opens new possibilities, since every photon generation attempt creates entanglement between the emitted photon and the magnetic sublevels of the atom, which is, e.g., useful for teleportation experiments [43] or the generation of entanglement between different platforms [44]. In [45], the properties of such a system are investigated and the creation of two-mode Schrödinger-cat states in the cavity is proposed.

2. Single-photon generation

For generating single photons, we make use of an adiabatic two-photon Raman process known as vSTIRAP [25]. The probability of receiving more than one photon per read pulse and emitter is practically zero, since the excitation laser frequency is far detuned from the emission frequency. But in order to identify the presence of more than one atom in the cavity mode, it is interesting to analyze the normalized cross-correlation $g_c^{(2)}(\Delta x)$ between photon detections in single photon counting module (SPCM) 1 and 2 of the Hanbury Brown–Twiss setup. If the individual SPCM i sees c_i counts in the 100 ns generation window m , $g_c^{(2)}$ is defined as

$$g_c^{(2)}(\Delta m) = \frac{1}{\bar{m}} \frac{\langle c_1(m) c_2(x + \Delta m) \rangle}{\langle c_1(m) \rangle \langle c_2(m) \rangle}, \quad (\text{A1})$$

where \bar{m} is the average number of coincidences for $\Delta m \neq 0$.

In Fig. 3, we show the detection coincidences for a shift of Δm windows along with the Poissonian error given by the number of coincidences. At $\Delta m = 0$, the dip is expected to reach zero for a perfect single-photon source [46,47], but it is usually limited by the dark count rates of the SPCMs and by Raman-scattered lock laser light [20]. These two effects are combined into the rates $x_{d_1} = (3.00 \pm 0.03)$ kcps and $x_{d_2} = (1.20 \pm 0.01)$ kcps in order to give the estimate

$$\begin{aligned} g_{c,\text{bg}}^{(2)}(0) &\approx \frac{\eta_{\text{retrieval}}(x_{d_1} + x_{d_2})}{(\eta_{\text{retrieval}}/2 + x_{d_1})(\eta_{\text{retrieval}}/2 + x_{d_2})} \\ &= (13.6 \pm 0.1)\%, \end{aligned}$$

which is derived from Eq. (A1) for equal SPCM detection efficiencies and the probability of detecting a photon per triggered pulse $\eta_{\text{retrieval}} = (2.3 \pm 0.1)\%$. Considering all g values in Fig. 5, we find $g_c^{(2)}(0) = (20.9 \pm 3.4)\%$, which means the contrast is not background limited, but most likely constrained by a small two-atom component. In order to filter the spurious events, we postselect the data for $g \in [70, 80] \times 2\pi$ MHz (highlighted bar in Fig. 5). As can be seen from Fig. 3, the value $g_c^{(2)}(0) = (12.2 \pm 6.5)\%$ is then close to the background limit, as expected. The bottleneck for giving more precise $g_c^{(2)}(0)$ estimates is the number of measurements.

APPENDIX B: THEORETICAL MODEL

1. Coherently driven multilevel atom in a dissipative cavity

First, we start with the more intuitive scenario of a closed system: The well-known Jaynes-Cummings Hamiltonian [48] describes the interaction between two atomic levels and a quantized mode of an electromagnetic field. We first extend this model to a three-level atom with two ground states $|g_1\rangle, |g_2\rangle$ and one excited state $|e\rangle$, where only the transition from $|g_2\rangle \rightarrow |e\rangle$ with frequency ω_{a_2} is resonant with the cavity. The Hamiltonian of this atom-cavity system consists of several parts:

$$\hat{H}_{\text{JC}} = \hat{H}_a + \hat{H}_c + \hat{H}_{\text{int}},$$

where \hat{H}_a and \hat{H}_c are the separate Hamiltonians of the atom and cavity mode, while \hat{H}_{int} describes the interaction.

We treat the atom-photon interaction in both dipole- and rotating-wave approximations, and simplify the individual

Hamiltonians by putting the dynamics in the frame of the pulse and Raman laser with frequencies $\omega_{p,R}$. The atom energy in the presence of a single-photon detuning $\Delta_{p-a} = \omega_p - \omega_{a_2}$ with respect to the excited state and a two-photon detuning $\delta = \Delta_{p-a} - (\omega_R - \omega_{a_1})$ with respect to the ground state $|g_1\rangle$ is given by

$$\hat{H}_a = -\hbar \Delta_{p-a} \cdot \hat{\sigma}_{ee} - \hbar \delta \cdot \hat{\sigma}_{g_1 g_1}. \quad (\text{B1})$$

We introduce the raising and lowering operators $\sigma_{kl}^\dagger = |l\rangle\langle k|$ and $\sigma_{kl} = |k\rangle\langle l|$, which describe the excitation and deexcitation of the atomic spin, respectively.

The energy of the cavity field can be expressed in analogy to the spectrum of a harmonic oscillator by m Fock states $|0\rangle, \dots, |m\rangle$. The creation- and annihilation operators \hat{a}^\dagger and \hat{a} add or remove a photon from the cavity mode with resonance frequency ω_c , so that its energy for a certain frequency detuning between the input pulse and cavity resonance $\Delta_{p-c} = (\omega_c - \omega_{a_2}) - \Delta_{p-a} = \Delta_{c-a} - \Delta_{p-a}$ reads

$$\hat{H}_c = -\hbar \Delta_{p-c} \cdot \hat{a}^\dagger \hat{a}.$$

In the following, we consider the special case $\Delta_{p-c} = \Delta_{p-a} = \delta = 0$.

The interaction term describes the coupling between the atomic dipole and the electric field of the cavity mode, which occurs with the Rabi frequency $2g$:

$$\hat{H}_{\text{int}} = i\hbar g (\hat{\sigma}_{g_2 e}^\dagger \hat{a} - \hat{\sigma}_{g_2 e} \hat{a}^\dagger). \quad (\text{B2})$$

We extend this model by two coherent, time-dependent driving terms, for which the overall Hamiltonian $\hat{H}(t)$ is given by

$$\hat{H}(t) = \hat{H}_{\text{JC}} + \hat{H}_d(t), \quad (\text{B3})$$

with the driving Hamiltonian

$$\hat{H}_d(t) = i\hbar \frac{\Omega(t)}{2} (\hat{\sigma}_{g_1 e}^\dagger - \hat{\sigma}_{g_1 e}) + \hbar \mathcal{E}(t) (\hat{a}^\dagger + \hat{a}). \quad (\text{B4})$$

The first term with $\Omega(t)$ stands for the control-laser-induced interaction in a Λ configuration. The control laser addresses the transition from ground to excited state, which is not coupled to the cavity. The second term populates the cavity mode according to the driving strength $\mathcal{E}(t)$.

Without dissipative processes, i.e., the interaction of our system with the environment, we cannot fully control the ground-state population of our system, as is intuitively clear from Eqs. (B4) and (B2): Any excitations brought into the system would lead to infinite oscillations between the states $|g_2\rangle$ and $|e\rangle$ as soon as the control laser does not realize a full population transfer to $|g_1\rangle$. The environmental states, on the other hand, are unknown, so we introduce the density matrix formalism and “open” our system to loss channels. The Schrödinger equation is replaced by the master equation [49], which describes the density matrix $\hat{\rho}$ of our closed system at any point in time:

$$\frac{d\hat{\rho}}{dt} = \hat{\mathcal{L}}\hat{\rho} = -\frac{i}{\hbar} [\hat{H}, \hat{\rho}] + \sum_l \hat{\mathcal{C}}_l \hat{\rho} \hat{\mathcal{C}}_l^\dagger - \frac{1}{2} (\hat{\mathcal{C}}_l^\dagger \hat{\mathcal{C}}_l \hat{\rho} + \hat{\rho} \hat{\mathcal{C}}_l^\dagger \hat{\mathcal{C}}_l). \quad (\text{B5})$$

The Liouvillian superoperator $\hat{\mathcal{L}}$ contains both the coherent dynamics given by Eq. (B3) and the Lindblad terms attributed

to the decay and loss channels, which are specified by the collapse operators $\hat{\mathcal{C}}_l$:

$$\hat{\mathcal{C}}_{\gamma_1} = \sqrt{2\gamma_1} \hat{\sigma}_{g_1 e}, \quad \hat{\mathcal{C}}_{\gamma_2} = \sqrt{2\gamma_2} \hat{\sigma}_{g_2 e}, \quad \hat{\mathcal{C}}_\kappa = \sqrt{2\kappa} \hat{a}. \quad (\text{B6})$$

The transmission rate κ_{HT} through the HT mirror and the unwanted damping of the field due to absorption, scattering at the mirrors, and leakage through the LT mirror at rate κ_{loss} form the total cavity loss rate $\kappa = \kappa_{\text{HT}} + \kappa_{\text{loss}}$. The excited-state decay $\Gamma = 2\gamma$ to both ground states is considered with independent rates $\gamma_{1,2}$ such that $\gamma = \gamma_1 + \gamma_2$.

The conversion of modes on the outside of a resonator to modes on the inside is commonly treated by the *input-output formalism* [50,51]. For mapping a weak coherent pulse with electric field probability amplitude $\phi_{\text{in}}(t)$ into the atom, we have to express the driving term $\mathcal{E}(t)$ in terms of $\phi_{\text{in}}(t)$, which contains on average n photons:

$$\mathcal{E}(t) = \sqrt{2\kappa_{\text{HT}}} \times \sqrt{n} \times \phi_{\text{in}}(t). \quad (\text{B7})$$

Here, we have considered that $\phi_{\text{in}}(t)$ has a temporal shape of length T , to which it is normalized such that $\int |\phi_{\text{in}}(t)|^2 dt = 1$, and a mean number of photons n . For a given $\phi_{\text{in}}(t)$ in the adiabatic storage regime, $\Omega(t)$ is found according to [18].

In summary, our model now describes the temporal evolution of an idealized, three-level atom coupled to a resonator, including losses as well as driven excitations. We can extract information, e.g., about the average intracavity photon number $\bar{n} = \langle \hat{a}^\dagger \hat{a} \rangle$, at any point in time. In the case of single-photon generation, the simulation provides predictions for $\mathcal{E}(t) = 0$. For our simulation plots, we solve Eq. (B5) to investigate the efficiency of coherent-pulse storage in dependence of its various parameters. For $t > T$, the system reaches a steady state ($\hat{\mathcal{L}}\hat{\rho} = 0$), which allows us to define the storage efficiency η_{storage} by the atomic state population in $|g_1\rangle$:

$$\eta_{\text{storage}} = \frac{\rho_{g_1 g_1}}{n} = \frac{\langle \hat{\sigma}_{g_1 g_1}^\dagger \hat{\sigma}_{g_1 g_1} \rangle}{n}. \quad (\text{B8})$$

Leaving the regime of weak coherent pulses with on average one photon ($n = 1$), we explore the dynamics in the limit $n \ll 1$. Remarkably, the results for η_{storage} then correspond exactly to the predictions for single-photon Fock-state storage in [14,18]: In the adiabatic storage regime of $TC\gamma \gg 1$, the storage efficiency is limited to

$$\eta_{\text{max}} = \frac{C}{C+1}, \quad (\text{B9})$$

where $C = \frac{g^2}{\kappa_{\text{HT}} \gamma}$ is the cooperativity parameter.

Reference [30], to our knowledge the most recent model to describe single-photon storage, is complex, as it involves the coupling of several electromagnetic modes inside and outside the resonator. Here, the excited-state decay is directed to an auxiliary state outside the three-level atom, most likely to quantify the free-space loss. The main new aspect of their work is an analysis of the drop in efficiency caused by *parasitic losses* (κ_{loss}). In their presence, a new limit for the optimum storage efficiency is found:

$$\eta'_{\text{max}} = \frac{\kappa_{\text{HT}}}{\kappa_{\text{HT}} + \kappa_{\text{loss}}} \frac{C'}{C' + 1}, \quad (\text{B10})$$

where $C' = \frac{g^2}{(\kappa_{\text{HT}} + \kappa_{\text{loss}})\gamma}$ is the loss-modified cooperativity. For $\kappa_{\text{loss}} \neq 0$, we obtain efficiencies according to Eq. (B10) as well. Also, in our model the population sum in all coherently coupled states is conserved, which is a more realistic case when considering adiabatic storage processes.

2. Four-level atom coupled to two cavity modes

In our tripod configuration, the mediating atomic excited state is coupled to two σ^\pm cavity modes. This means an additional state $|g_3\rangle$ of approximately equal energy, as $|g_2\rangle$ has to be taken into account [see Fig. 1(c)]. The corresponding operators acting on the photon number in the second cavity mode are \hat{b}^\dagger and \hat{b} . Thus we modify the interaction Hamiltonian in Eq. (B2) and the collapse operators in Eq. (B6) to

$$\hat{H}'_{\text{int}} = i\hbar g(\hat{\sigma}_{g_2e}^\dagger \hat{a} - \hat{\sigma}_{g_2e} \hat{a}^\dagger) + i\hbar g'(\hat{\sigma}_{g_3e}^\dagger \hat{b} - \hat{\sigma}_{g_3e} \hat{b}^\dagger) \quad (\text{B11})$$

and

$$\begin{aligned} \hat{C}'_{\gamma'_1} &= \sqrt{2\gamma'_1} \hat{\sigma}_{g_1,e}, & \hat{C}'_{\gamma'_2} &= \sqrt{2\gamma'_2} \hat{\sigma}_{g_2,e}, \\ \hat{C}'_{\gamma_3} &= \sqrt{2\gamma_3} \hat{\sigma}_{g_3,e}, & \hat{C}'_{\kappa_a} &= \sqrt{2\kappa} \hat{a}, & \hat{C}'_{\kappa_b} &= \sqrt{2\kappa} \hat{b}, \end{aligned}$$

with the new coupling strength g' and an adjusted branching ratio of the excited-state decays γ_3 and $\gamma'_{1,2}$. In reality, there are more levels to decay to, but their respective transitions strengths are weak, such that we may neglect them. Additionally, the excited-state population decay is very small at any time ($\kappa \gg \gamma_i$).

The cooperativity parameter C is defined for a single atom-cavity coupling rate only. We are not aware of any generalized coupling parameter depending on g and g' , so we cannot estimate the efficiency as in Eq. (B10). Instead, we only give results based on our simulations.

3. Multiple excited states

We assume transform-limited pulses, i.e., for our given pulse duration and shape, a minimum spectral width is implied. However, the width can easily be on the order of the frequency difference of neighboring atomic excited states. As a consequence, multiple excited states have to be taken into account. For ^{87}Rb , the Raman laser addressing the $|F=1, m_F=-1\rangle \rightarrow |F'=2, m_F=-1\rangle$ transition has a nonzero probability of driving the $\Delta = 157$ MHz red-detuned $|F=2, m_F=-2\rangle \rightarrow |F'=1, m_F=-1\rangle$ transition, which is why the state $|f\rangle = |F'=1, m_F=-1\rangle$ should be taken into account. The cavity itself acts as a frequency filter for the input pulse, reducing the probability for off-resonant transitions to less than a relative 2.5%.

In our simulation we include multilevel-atom effects by introducing the detuned excited state with energy

$$\hat{H}_a = -\hbar \Delta \cdot \hat{\sigma}_{ff} \quad (\text{B12})$$

and extending Eq. (B4) to

$$\begin{aligned} \hat{H}'_d(t) &= i\hbar \frac{\Omega(t)}{2} (\hat{\sigma}_{g_1e}^\dagger - \hat{\sigma}_{g_1e}) + \hbar \mathcal{E}(t) (\hat{a}^\dagger + \hat{a}) \\ &+ i\hbar \frac{\Omega'(t)}{2} (\hat{\sigma}_{g_1f}^\dagger - \hat{\sigma}_{g_1f}) \end{aligned}$$

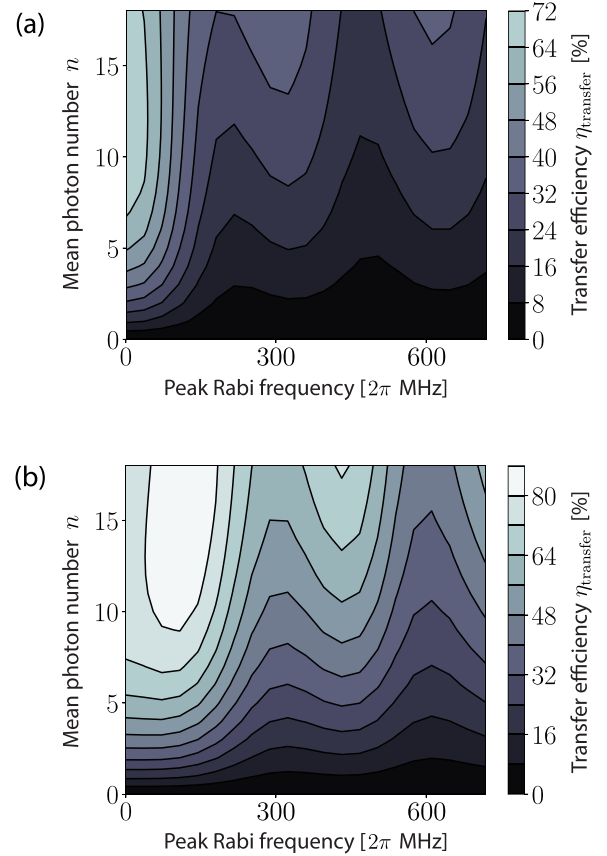


FIG. 6. Figure 4(b) shows the population transfer η_{transfer} to $|F, m_F\rangle = |1, -1\rangle$ as a function of the mean input pulse photon number n and the control pulse peak Rabi frequency. Here, plot (a) shows the transfer to $|2, 0\rangle$, while plot (b) displays the sum of the transfer efficiencies to both states. The total transfer reaches above 80%, in agreement with the expectation for large n .

and Eq. (B11) to

$$\begin{aligned} \hat{H}''_{\text{int}} &= i\hbar g(\hat{\sigma}_{g_2e}^\dagger \hat{a} - \hat{\sigma}_{g_2e} \hat{a}^\dagger) + i\hbar g'(\hat{\sigma}_{g_3e}^\dagger \hat{b} - \hat{\sigma}_{g_3e} \hat{b}^\dagger) \\ &+ i\hbar g''(\hat{\sigma}_{g_2f}^\dagger \hat{a} - \hat{\sigma}_{g_2f} \hat{a}^\dagger) + i\hbar g'''(\hat{\sigma}_{g_3f}^\dagger \hat{b} - \hat{\sigma}_{g_3f} \hat{b}^\dagger), \end{aligned}$$

where $\Omega'(t)$, g'' , and g''' are the new coupling strengths obtained by the ratio of Clebsch-Gordan coefficients. The decay rates and collapse operators are adjusted as well. This is finally the model we use to interpret our measured data.

The main effect of an additional excited state $|1', -1\rangle$ is that a small fraction of the population in the target state $|1, -1\rangle$ is transferred to the excited state and back during the storage process. These dynamics result in a slightly reduced expected efficiency compared to a simplified four-level atom approach. However, for well-controlled polarizations of the manipulating beams and cavity modes, five states are sufficient to describe a real multilevel atom, since the $F'=3$ level does not couple to the target ground state. Additionally, it is not addressed by the input pulse, which is frequency-filtered by the cavity.

4. On the maximum achievable transfer efficiency

In Fig. 4(b), the maximum achievable transfer efficiency is limited to slightly above 60%, even for high-input photon numbers. The transfer efficiency regards transfer only to $|1, -1\rangle$ and neglects the population in the undesired state $|2, 0\rangle$. In Fig. 6 the transfer to $|2, 0\rangle$ is shown, as well as the sum of the transfers to both states. The combined transfer reaches above 80%, a value which might converge towards 100% for even higher mean photon numbers [52]. However, simulations for several tens of Fock states and a five-level atom are computationally challenging. Intuitively, it is clear that cavity field dampings due to both κ_{loss} and κ_{HT} can be compensated by sending larger input fields. But the coherent population leakage in a tripod configuration will always take place, reducing the efficiency of transfer to the target state.

5. Numerical tools

Exact analytical solutions to the master equation (B5) are only possible in special cases. In general, a numerical approach is the easier choice. We use QUTIP (v4.1), the quantum toolbox in PYTHON (v3.5) [53,54], to facilitate the process of setting up state vectors, time-(in)dependent Hamiltonians, and (super-)operators and to solve Eq. (B5) with the in-built function *mesolve*. Based on an ordinary differential equation solver, it evolves the density matrix and returns a time-binned array of expectation values for a list of operators. As a result, for example, the shape of generated photons can be simulated.

In order to fit these shapes and to obtain the system parameters, we developed our own optimal control scheme based on

basin hopping. Basin hopping [55] is a stochastic algorithm which is similar to the well-known *simulated annealing* (SA) algorithm. As opposed to gradient-based search algorithms, it is less liable to end up in a local minimum while determining the global minimum of a cost function in a large parameter space.

The algorithm iterates through cycles composed of random perturbation of the parameters, local optimization by a routine to be specified, and acceptance or rejection of the parameter set P based on the cost function value. We apply the *Nelder-Mead method* [56], also known as the *downhill simplex method*, for the local optimization. Based on the concept of simplices, it approximates local optima by evaluating cost values along the $P + 1$ points of a volume and introducing variations such that the cost value decreases. For fitting the photon shape, we define the cost function $\mathcal{C}_{\text{retrieval}}$ as

$$\mathcal{C}_{\text{retrieval}} = \bar{n}_{\text{exp}}(t) - n_0 \cdot \bar{n}[t, \tau_{\Omega}, \Omega(t), \Delta, g_{\text{dist}}], \quad (\text{B13})$$

where the average photon number $\bar{n}(t)$ given by the simulation depends on the value of $\Delta = \Delta_{\text{p-a}}$ and the driving Rabi frequency $\Omega(t)$ and its pulse delay τ_{Ω} . The experimentally determined variation in coupling strengths is implemented as a distribution g_{dist} [as in Fig. 5(a)], over which we average along with the different initial m_F ground states. \bar{n} is scaled with n_0 in order to reduce the difference of $\bar{n}(t)$ and the measured average detector counts $\bar{n}_{\text{exp}}(t)$. Once the simulation finds the parameters to recreate $\bar{n}_{\text{exp}}(t)$, we can estimate the efficiency of photon generation by integrating over the intracavity photon number.

-
- [1] P. Kok, W. J. Munro, K. Nemoto, T. C. Ralph, J. P. Dowling, and G. J. Milburn, *Rev. Mod. Phys.* **79**, 135 (2007).
 - [2] J. I. Cirac, A. K. Ekert, S. F. Huelga, and C. Macchiavello, *Phys. Rev. A* **59**, 4249 (1999).
 - [3] N. Sangouard, C. Simon, H. de Riedmatten, and N. Gisin, *Rev. Mod. Phys.* **83**, 33 (2011).
 - [4] H. J. Briegel, W. Dür, J. I. Cirac, and P. Zoller, *Phys. Rev. Lett.* **81**, 5932 (1998).
 - [5] L.-M. Duan, M. D. Lukin, J. I. Cirac, and P. Zoller, *Nature (London)* **414**, 413 (2001).
 - [6] J. I. Cirac, P. Zoller, H. J. Kimble, and H. Mabuchi, *Phys. Rev. Lett.* **78**, 3221 (1997).
 - [7] T. E. Northup and R. Blatt, *Nat. Photonics* **8**, 356 (2014).
 - [8] M. Körber, O. Morin, S. Langenfeld, A. Neuzner, S. Ritter, and G. Rempe, *Nat. Photonics* **12**, 18 (2018).
 - [9] A. D. Boozer, A. Boca, R. Miller, T. E. Northup, and H. J. Kimble, *Phys. Rev. Lett.* **98**, 193601 (2007).
 - [10] H. P. Specht, C. Nölleke, A. Reiserer, M. Uphoff, E. Figueroa, S. Ritter, and G. Rempe, *Nature (London)* **473**, 190 (2011).
 - [11] R. Keil, M. Zopf, Y. Chen, B. Höfer, J. Zhang, F. Ding, and O. G. Schmidt, *Nat. Commun.* **8**, 15501 (2017).
 - [12] D. C. Burnham and D. L. Weinberg, *Phys. Rev. Lett.* **25**, 84 (1970).
 - [13] D. Hunger, T. Steinmetz, Y. Colombe, C. Deutsch, T. W. Hänsch, and J. Reichel, *New J. Phys.* **12**, 065038 (2010).
 - [14] A. V. Gorshkov, A. André, M. D. Lukin, and A. S. Sørensen, *Phys. Rev. A* **76**, 033804 (2007).
 - [15] A. V. Gorshkov, A. André, M. D. Lukin, and A. S. Sørensen, *Phys. Rev. A* **76**, 033805 (2007).
 - [16] M. Steiner, V. Leong, M. A. Seidler, A. Cerè, and C. Kurtsiefer, *Opt. Express* **25**, 6294 (2017).
 - [17] M. Fleischhauer, S. Yelin, and M. Lukin, *Opt. Commun.* **179**, 395 (2000).
 - [18] J. Dilley, P. Nisbet-Jones, B. W. Shore, and A. Kuhn, *Phys. Rev. A* **85**, 023834 (2012).
 - [19] J. Gallego, W. Alt, T. Macha, M. Martínez-Dorantes, D. Pandey, and D. Meschede, *Phys. Rev. Lett.* **121**, 173603 (2018).
 - [20] J. Gallego, S. Ghosh, S. K. Alavi, W. Alt, M. Martínez-Dorantes, D. Meschede, and L. Ratschbacher, *Appl. Phys. B* **122**, 47 (2016).
 - [21] M. Martínez-Dorantes, W. Alt, J. Gallego, S. Ghosh, L. Ratschbacher, Y. Völzke, and D. Meschede, *Phys. Rev. Lett.* **119**, 180503 (2017).
 - [22] S. Kuhr, W. Alt, D. Schrader, M. Müller, V. Gomer, and D. Meschede, *Science* **293**, 278 (2001).
 - [23] R. Reimann, W. Alt, T. Macha, D. Meschede, N. Thau, S. Yoon, and L. Ratschbacher, *New J. Phys.* **16**, 113042 (2014).
 - [24] A. Neuzner, S. Dürr, M. Körber, S. Ritter, and G. Rempe, *Phys. Rev. A* **98**, 013401 (2018).

- [25] M. Mücke, J. Bochmann, C. Hahn, A. Neuzner, C. Nölleke, A. Reiserer, G. Rempe, and S. Ritter, *Phys. Rev. A* **87**, 063805 (2013).
- [26] P. B. R. Nisbet-Jones, J. Dille, D. Ljunggren, and A. Kuhn, *New J. Phys.* **13**, 103036 (2011).
- [27] M. Keller, B. Lange, K. Hayasaka, W. Lange, and H. Walther, *Nature (London)* **431**, 1075 (2004).
- [28] B. W. Shore and P. L. Knight, *J. Mod. Opt.* **40**, 1195 (1993).
- [29] N. V. Vitanov, A. A. Rangelov, B. W. Shore, and K. Bergmann, *Rev. Mod. Phys.* **89**, 015006 (2017).
- [30] L. Giannelli, T. Schmit, T. Calarco, C. P. Koch, S. Ritter, and G. Morigi, *New J. Phys.* **20**, 105009 (2018).
- [31] B. W. Shore, *Adv. Opt. Photonics* **9**, 563 (2017).
- [32] G. K. Gulati, H. Takahashi, N. Podoliak, P. Horak, and M. Keller, *Sci. Rep.* **7**, 5556 (2017).
- [33] H. J. Kimble, *Nature (London)* **453**, 1023 (2008).
- [34] A. Reiserer and G. Rempe, *Rev. Mod. Phys.* **87**, 1379 (2015).
- [35] K. T. Kaczmarek, P. M. Ledingham, B. Brecht, S. E. Thomas, G. S. Thekkadath, O. Lazo-Arjona, J. H. D. Munns, E. Poem, A. Feizpour, D. J. Saunders, J. Nunn, and I. A. Walmsley, *Phys. Rev. A* **97**, 042316 (2018).
- [36] M. R. Sprague, P. S. Michelberger, T. F. M. Champion, D. G. England, J. Nunn, X.-M. Jin, W. S. Kolthammer, A. Abdolvand, P. S. J. Russell, and I. A. Walmsley, *Nat. Photonics* **8**, 287 (2014).
- [37] S. Welte, B. Hacker, S. Daiss, S. Ritter, and G. Rempe, *Phys. Rev. X* **8**, 011018 (2018).
- [38] R. J. Thompson, G. Rempe, and H. J. Kimble, *Phys. Rev. Lett.* **68**, 1132 (1992).
- [39] H. M. Meyer, R. Stockill, M. Steiner, C. Le Gall, C. Matthiesen, E. Clarke, A. Ludwig, J. Reichel, M. Atatüre, and M. Köhl, *Phys. Rev. Lett.* **114**, 123001 (2015).
- [40] M. Zopf, T. Macha, R. Keil, E. Uruñuela, Y. Chen, W. Alt, L. Ratschbacher, F. Ding, D. Meschede, and O. G. Schmidt, *Phys. Rev. B* **98**, 161302(R) (2018).
- [41] R. Gehr, J. Volz, G. Dubois, T. Steinmetz, Y. Colombe, B. L. Lev, R. Long, J. Estève, and J. Reichel, *Phys. Rev. Lett.* **104**, 203602 (2010).
- [42] A. Boca, R. Miller, K. M. Birnbaum, A. D. Boozer, J. McKeever, and H. J. Kimble, *Phys. Rev. Lett.* **93**, 233603 (2004).
- [43] C. Nölleke, A. Neuzner, A. Reiserer, C. Hahn, G. Rempe, and S. Ritter, *Phys. Rev. Lett.* **110**, 140403 (2013).
- [44] M. Lettner, M. Mücke, S. Riedl, C. Vo, C. Hahn, S. Baur, J. Bochmann, S. Ritter, S. Dürr, and G. Rempe, *Phys. Rev. Lett.* **106**, 210503 (2011).
- [45] M. W. Janowicz and J. M. A. Ashbourn, *Phys. Rev. A* **55**, 2348 (1997).
- [46] H. J. Kimble, M. Dagenais, and L. Mandel, *Phys. Rev. Lett.* **39**, 691 (1977).
- [47] H. Paul, *Rev. Mod. Phys.* **54**, 1061 (1982).
- [48] E. Jaynes and F. Cummings, *Proc. IEEE* **51**, 89 (1963).
- [49] H. J. Carmichael, *Statistical Methods in Quantum Optics I: Master Equations and Fokker-Planck Equations* (Springer, New York, 2002).
- [50] D. F. Walls and G. J. Milburn, *Quantum Optics* (Springer Science & Business Media, New York, 2007).
- [51] M. Aspelmeyer, T. J. Kippenberg, and F. Marquardt, *Rev. Mod. Phys.* **86**, 1391 (2014).
- [52] We have confirmed this behavior in the adiabatic regime for a Λ configuration.
- [53] J. Johansson, P. Nation, and F. Nori, *Comput. Phys. Commun.* **184**, 1234 (2013).
- [54] J. Johansson, P. Nation, and F. Nori, *Comput. Phys. Commun.* **183**, 1760 (2012).
- [55] D. Wales, *Energy Landscapes: Applications to Clusters, Biomolecules and Glasses* (Cambridge University Press, Cambridge, England, 2003).
- [56] F. Gao and L. Han, *Comput. Optim. Appl.* **51**, 259 (2012).